ACS APPLIED MATERIALS & INTERFACES

May 29, 2024
Volume 16
Number 21
pubs.acs.org/acsami

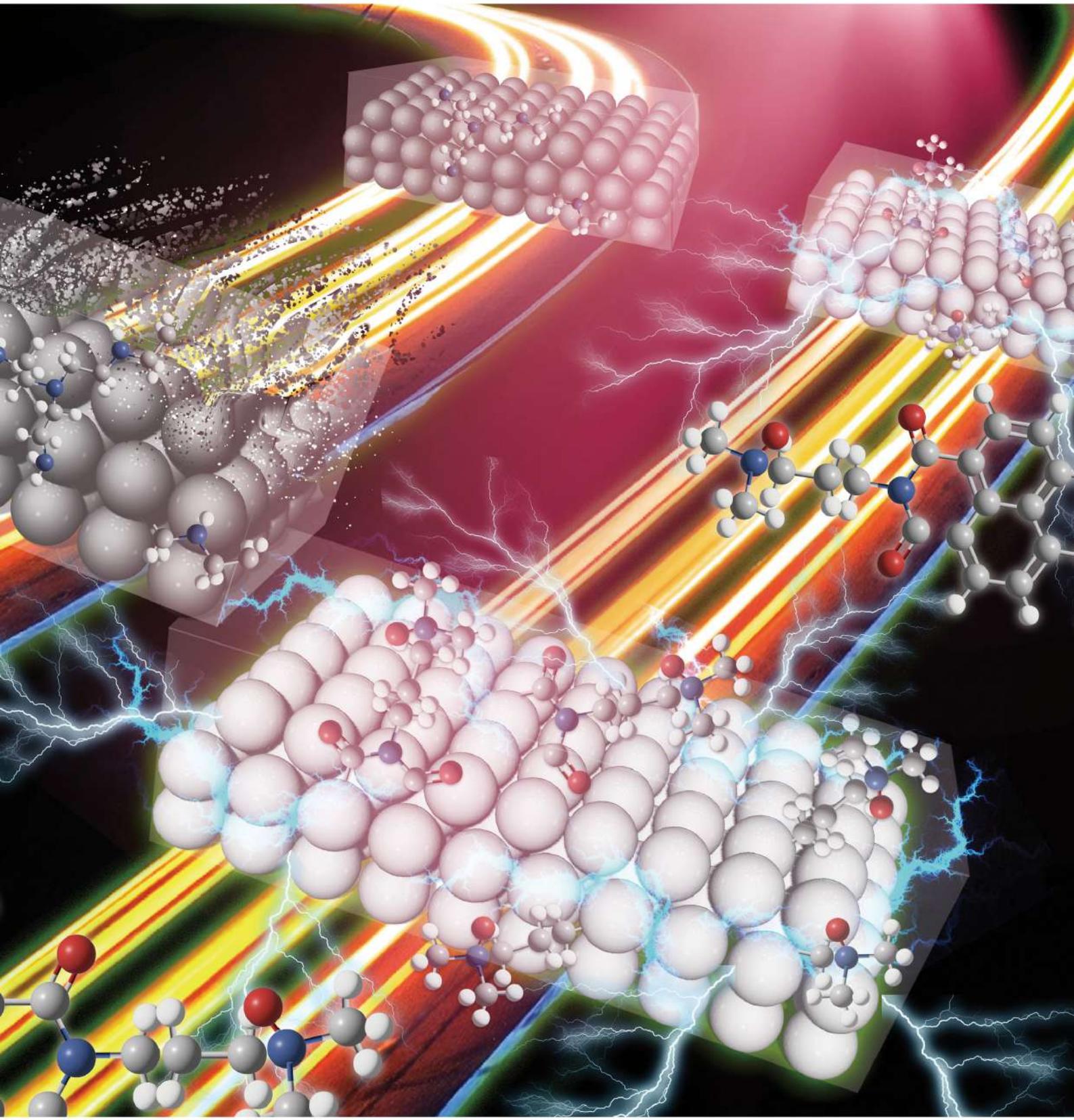

ACS Publications
Most Trusted. Most Cited. Most Read.

www.acs.org

ACS APPLIED MATERIALS & INTERFACES

www.acsami.org

Research Article

Advancing Detectivity and Stability of Near-Infrared Organic Photodetectors via a Facile and Efficient Cathode Interlayer

Yu-Ching Huang,* Tai-Yuan Wang, Zhi-Hao Huang, and Svette Reina Merden Solante Santiago

Cite This: *ACS Appl. Mater. Interfaces* 2024, 16, 27576−27586

Read Online

ACCESS | Metrics & More | Article Recommendations | Supporting Information

ABSTRACT: Near-infrared (NIR) organic photodetectors (OPDs) are pivotal in numerous technological applications due to their excellent responsivity within the NIR region. Polyethylenimine ethoxylated (PEIE) has conventionally been employed as an electron transport layer (hole-blocking layer) to suppress dark current (J_D) and enhance charge transport. However, the limitations of PEIE in chemical stability, processing conditions, environmental impact, and absorption range have spurred the development of alternative materials. In this study, we introduced a novel solution: a hybrid of sol−gel zinc oxide (ZnO) and *N*,*N*′-bis(*N*,*N*-dimethylpropan-1-amine oxide)perylene-3,4,9,10-tetracarboxylic diimide (PDINO) as the electron transport layer for NIR-OPDs. Our fabricated OPD exhibited significantly improved responsivity, reduced internal traps, and enhanced charge transfer efficiency. The detectivity, spanning from 400 to 1100 nm, surpassed ∼5 × 10^{12} Jones, reaching ∼1.1 × 10^{12} Jones at 1000 nm, accompanied by an increased responsivity of 0.47 A/W. Also, the unpackaged OPD remarkedly demonstrated stable J_D and external quantum efficiency (EQE) over 1000 h under dark storage conditions. This innovative approach not only addresses the drawbacks of conventional PEIE-based OPDs but also offers promising avenues for the development of high-performance OPDs in the future.

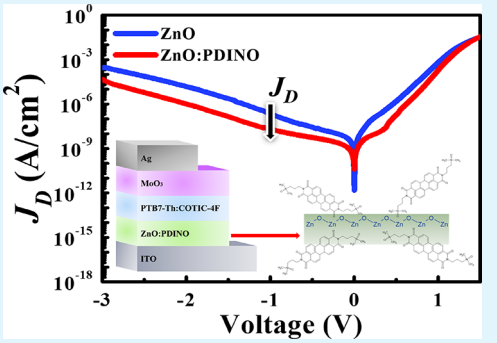

KEYWORDS: *near-infrared organic photodetectors, PDINO, electron transport layer, charge transport, dark current*

1. INTRODUCTION

Near-infrared (NIR) photodetectors (PDs) are state-of-the-art devices for optical communication, environmental monitoring, biomedical imaging, and sensing.[1,2] Most of the commercially available NIR-PDs are typically made from inorganic semiconductor materials such as silicon (Si), germanium (Ge), indium gallium arsenide (InGaAs), and lead sulfide (PbS).[3,4] Inorganic PDs (IPDs) offer high responsivities and detectivity, cover a broad range of wavelengths, and exhibit good stability and reliability over time.[5] However, high cost, low optical absorption, and complex manufacturing processes limit the successive development of IPDs.[6] In contrast, NIR organic photodetectors (OPDs) demonstrate low cost, optical tunability, and solution processability that have extensively overcome the IPDs' drawbacks.[7,8]

The NIR-OPD involves a bulk heterostructure junction (BHJ) formed by blending a donor material and an acceptor material to act as a light absorber layer that generates charge carriers. Typically, the donor materials are conjugated polymers[7,9] or small molecules[10,11] while the acceptor materials are mainly fullerene derivatives and nonfullerene small molecules. Recently, many novel nonfullerene acceptor (NFA) materials[12,13] have shown excellent absorption characteristics in the wavelength ranging from 900 to 1000 nm, such as COI-4F, COI-4Cl, IEICO-4F,[14] COTIC-4F,[12,15] and COTIC-4Cl.[16] These materials enable the external quantum efficiency (EQE) of the OPD to increase to levels close to that of the Si-based PD. However, as the absorption spectra of the material shift to the NIR light region, the carriers would be more easily injected due to its narrow energy level, also increasing the dark current (J_D) by several orders of magnitude.[9,17] However, a low J_D is essential to obtaining high detectivity for OPDs.[18] To effectively suppress the J_D, varying methods have been proposed, such as adding barrier layers,[10,14] reducing the interfacial defect density,[13,19] enhancing the active layer thickness,[20] and using the inverted structure.[21] Huang et al.[9] reduced the J_D from 2 × 10^{-7} to 7 × 10^{-9} A/cm^2 at −2 V, by increasing the thickness of the active layer, while the thick active layer led to a reduction in EQE from 65 to 59% at a wavelength of 940 nm. They then increased the injection barrier by adding CuSCN as an electron-blocking layer to modulate the J_D at −0.1 V from 2.3 × 10^{-8} to 2.7 × 10^{-10} A/cm^2. On the other hand, Xu et al.[22] induced Y6 as an interfacial layer by solvent vapor annealing to reduce the interface defects, resulting in a reduced J_D from 1.9

Received: January 25, 2024
Revised: April 26, 2024
Accepted: April 30, 2024
Published: May 9, 2024

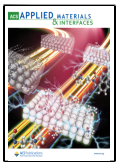

https://doi.org/10.1021/acsami.4c01466
ACS Appl. Mater. Interfaces 2024, 16, 27576−27586

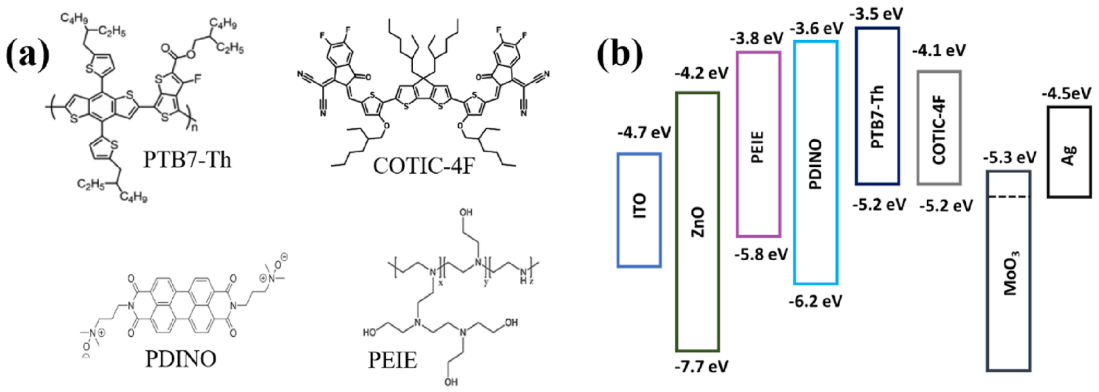

Figure 1. (a) Chemical structures of PTB7-Th, COTIC-4F, PDINO, and PEIE. (b) Schematic energy band diagram of the OPD device.

$\times 10^{-6}$ to 1.2×10^{-9} A/cm^2 at −0.1 V. Although the generation of J_D can be prevented at low bias voltages (< −0.5 V) by employing an interfacial layer, J_D increases significantly with increasing bias voltage. Zinc oxide (ZnO) is the most common electron transport layer (ETL) material in the inverted-structure OPDs and organic photovoltaics (OPVs), which is inexpensive and has strong mobility, and thus is frequently utilized for J_D modulation.[23] However, oxygen vacancies in ZnO tend to increase J_D because of electron injection, making it crucial to substitute the vacancies with other materials to reduce the J_D. A variety of materials such as PFN-Br,[24] LiF,[25] BCP,[26] Bphen,[27] and PEIE[28] have been employed as a hybrid to ZnO. Recently, the team led by Li[13] demonstrated reducing interface defects by blending PEIE with ZnO. Since the nitrogen element in PEIE fills the oxygen vacancies in ZnO, the lowest J_D is effectively achieved at 1.91×10^{-9} A/cm^2 at −1 V. Nonetheless, the C═O bond in the NFAs will react with the amine group in PEIE, destroying the original electrical structure of the NFAs. This effect consequently reduces the stability of the OPD,[29−31] and the insulating properties of PEIE itself also require precise control of the thickness and concentration.[32−34] For these reasons, it is necessary to choose a material to replace PEIE to fill in the oxygen vacancies in ZnO. In recent OPV studies, *N*,*N*′-bis(*N*,*N*-dimethylpropan-1-amine oxide)perylene-3,4,9,10-tetracarboxylic diimide (PDINO) is found to be a potential material as an ETL due to its amino N-oxide group with strong electron affinity, electron mobility, and a π-delocalized planar structure.[34,35] PDINO is mostly used as a cathode interlayer in conventional-structure OPVs and is rarely used in inverted-structure OPVs. Marsal et al.[35] provided a systematic analysis for the stability of inverted OPVs with different ETLs, and their results demonstrate that the OPVs have superior photostability by replacing ZnO with PDINO as a cathode interlayer. However, the performance influencing factors in OPVs and OPDs are different and the relevant potential of PDINO in inverted NIR-OPDs is still unexplored.

In this work, we demonstrate the optimization of the ETL with ZnO to achieve a high-performance NIR-OPD, by forming a hybrid layer with the small-molecule PDINO to reduce the oxygen defects and suppress the J_D. The blend of poly{4,8-bis[5-(2-ethylhexyl)thiophen-2-yl]benzo[1,2-*b*:4,5-*b*′]-dithiophene-2,6-diyl-*alt*-3-fluoro-2-[(2-ethylhexyl)-carbonyl]-thieno[3,4-*b*]thiophene-4,6-diyl} (PTB7-Th) and COTIC-4F was used as the active layer in this study. For the reduction of J_D, due to the hybrid of PDINO with ZnO, the work function of ZnO is reduced from ∼4.79 to ∼4.68 eV, which consequently increases its injection barrier by 0.11 eV, and finally reduces the J_D from 2.1×10^{-7} to 2.1×10^{-8} A/cm^2 at −1 V. Notably, the EQE has maintained ∼50% with a high light response at 1000 nm, therefore increasing its specific detectivity obtained from noise current (D_n*) to 1.1×10^{12} Jones. This D_n* is also the highest value under the same operating conditions in the PTB7-COTIC-4F system in the current literature, indicating that the PDINO modification indeed improves the detecting performance considerably. Furthermore, the OPDs with PDINO-modified ETL exhibit excellent stability. Under 1000 h of dark storage, the J_D of the PEIE-modified OPDs increased by two orders of magnitude while the J_D of the PDINO-modified OPDs remained almost unchanged. Our study demonstrates a new type of ETL structure that has great potential to achieve high-performance NIR-OPD.

2. METHODOLOGY

2.1. Materials. PTB7-Th, COTIC-4F, and PDINO were purchased from 1-Material Inc. Zinc acetate was obtained from Alfa Aesar. 2-Methoxylethanol, ethanolamine, chlorobenzene (CB), *ortho*-xylene (*o*-xylene), 1-chloronaphthalene (CN), MoO_3, and PEIE were availed from Sigma-Aldrich. All reagents and solvents were used without further purification. The chemical structures of PTB7-Th, COTIC-4F, PDINO, and PEIE are presented in Figure 1a. ZnO was synthesized through the sol−gel method, according to a previous report.[18] Here, the PDINO solution was prepared at 0.5 mg/mL in methanol and the PEIE solution was diluted in 2-methoxyethanol prepared into 0.4 wt % of solution. For the hybrid ETLs, the sol−gel ZnO precursor was mixed with different volume ratios of PDINO or PEIE solutions.

2.2. Device Fabrication. The OPD was fabricated on commercially available indium tin oxide (ITO)/glass substrate that was precleaned through ultrasonication in deionized water, acetone, and isopropanol consecutively each for 30 min. The as-prepared ZnO was deposited at a spin coating rate of 3000 rpm for 30 s on the ITO/glass substrate, followed by annealing treatment at 180 °C for 20 min. Here, the introduction of PDINO and PEIE was done in two methods. The first method involved the one-step hybridization of PDINO and PEIE separately with ZnO in a sol−gel solution; the devices are herein labeled as ZnO:PDINO and ZnO:PEIE, respectively. The second method involved the deposition of PDINO and PEIE separately on the ZnO layer (demonstrating a two-step bilayer process), effectively serving as an interfacial layer on the ETL; the devices are herein named ZnO/PDINO

https://doi.org/10.1021/acsami.4c01466
ACS Appl. Mater. Interfaces 2024, 16, 27576−27586

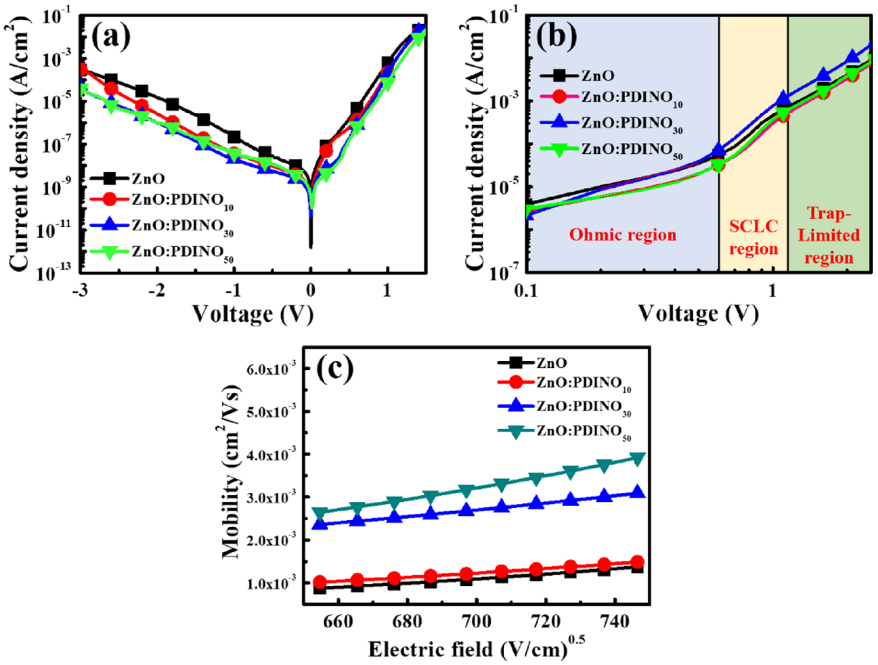

Figure 2. (a) J_D-V curves, (b) SCLC plots, and (c) calculated electron mobilities of OPDs with various ZnO:PDINO ETLs at different hybrid ratios of 0, 10, 30, and 50 vol % of PDINO.

and ZnO/PEIE, respectively. Subsequently, the substrates were transferred to an N_2-filled glovebox. The PTB7-Th:COTIC-4F active layer solution (20 mg/mL in *o*-xylene and *o*-xylene with 0.5 vol % CN) was stirred at 65 °C for 12 h in a glovebox. This active layer solution was spin-coated on the ETL at 3000 rpm for 30 s in a glovebox. Additionally, MoO_3 (5 nm, HTL) and Ag (100 nm) were successively deposited on the active layer through thermal evaporation. The final OPD area is 0.04 cm^2, and the energy band diagram of the OPD structure is demonstrated in Figure 1b.

2.3. Characterization. The film thickness was measured using Alpha-stepper (Bruker). The morphology and roughness of the film surface were measured using atomic force microscopy (AFM; Bruker). The work function of the film was measured using the scanning kelvin probe (KP Technology SKP5050), which is a surface analyzer used to directly measure work function differences and surface potential variations on solid surfaces. The J_D-voltage (J_D-V) characteristics of the devices were recorded using a Keithley 2400 source meter. EQE spectra and responsivities at wavelengths ranging 300−1200 nm were recorded in DC mode using a QE-R system (Enlitech, Taiwan) and a Si-based PD (Hamamatsu S1337), which was employed programmatically to calibrate the monochromatic beam, according to the IEC 60904-8:20146 standard. The ultraviolet−visible (UV−vis) spectrophotometer (Jasco V-750) was used to measure the absorption behavior and calculate the bandgap energy of the active layer. The current density−voltage ($J-V$) characteristics and the noise current were recorded using a programmable source meter (Keithley, model 2636A) in the dark. The photocurrent response to the light intensity was measured through the evaluation of the linear dynamic range (LDR). To measure the LDR, light-emitting diode (LED; Thorlabs, M940L2) beams with a wavelength of 940 nm were pointed at a motor-driven filter wheel (Thorlabs, FW102CNEB) to produce a controlled light intensity over the area of the OPD device. The frequency response of the OPD was measured by using a commercial LED (Thorlabs) having a luminous flux density of 1 mW/cm^2 at 940 nm, connected to a function generator (Tektronix, AFG3102C) to generate a pulse to trigger the OPDs. The output pulse of the OPD was amplified by a preamplifier operated at a low noise current with an A/V gain factor of 10^{-6}; the amplified output pulse was then captured and plotted by a 2.5 GHz oscilloscope (Teledyne LeCroy, WaveRunner 625Zi). Electrochemical impedance spectroscopy (EIS; Solartron, Materials Lab XM) was used to analyze sinusoidal AC signals in the 10^{-1} to 1 MHz sweep mode with an amplitude of 1 V, while the defect density and charge mobility were calculated by space-charge-limited current (SCLC). The extraction time and recombination rate of the charge carriers were obtained from transient photovoltage (TPV) and transient photocurrent (TPC) measurements, using a Paios 4.0 instrument (FLUXiM AG, Switzerland). Highly sensitive EQE was measured using an integrated Fourier-transform photocurrent spectroscopy system (FTPS, Enlitech), where the photocurrent was amplified and modulated by a lock-in instrument. EL_{EQE} measurements were performed by applying external voltage/current sources through the devices (REPS+, Enlitech). All of the devices were prepared for EL_{EQE} measurements according to the optimal device fabrication conditions. EL_{EQE} measurements were carried out from 0 to 3 V.

3. RESULTS AND DISCUSSION

ZnO can be used as an ETL and an interface layer at the same time; however, the oxygen vacancies in the film become the main source of charge tunneling under reverse bias, resulting in a large amount of current leakage and reduction of the detecting performance. To suppress the generation of leakage current, we first hybrid PDINO in ZnO (ZnO:PDINO) to reduce the formation of oxygen defects. Figure 2a shows the J_D-V curves of ZnO:PDINO at different hybrid ratios of 0, 10, 30, and 50 vol % of PDINO, named ZnO, ZnO:PDINO$_{10}$, ZnO:PDINO$_{30}$, and ZnO:PDINO$_{50}$, respectively. It is shown

https://doi.org/10.1021/acsami.4c01466
ACS Appl. Mater. Interfaces 2024, 16, 27576−27586

Table 1. Calculated Values of J_D, μ_e, V_{TFL}, and N_t of OPDs with Various ZnO:PDINO ETLs at Hybrid Ratios of 0, 10, 30, and 50 vol% of PDINO

ETL	J_D(A/cm^2)[a]	μ_e(cm^2 V^{-1} s^{-1})	V_{TFL}(V)	N_t(cm^{-3})
ZnO	2.1×10^{-7} ($2.4 \pm 0.3 \times 10^{-7}$)	1.1×10^{-4}	0.69	7.7×10^{15}
ZnO:PDINO$_{10}$	3.6×10^{-8} ($3.8 \pm 0.2 \times 10^{-8}$)	1.2×10^{-4}	0.67	6.2×10^{15}
ZnO:PDINO$_{30}$	2.1×10^{-8} ($2.3 \pm 0.2 \times 10^{-8}$)	3.2×10^{-4}	0.61	2.7×10^{15}
ZnO:PDINO$_{50}$	3.7×10^{-8} ($4.0 \pm 0.3 \times 10^{-8}$)	2.7×10^{-4}	0.65	5.2×10^{15}

[a]The average data are obtained from 10 devices for each ETL.

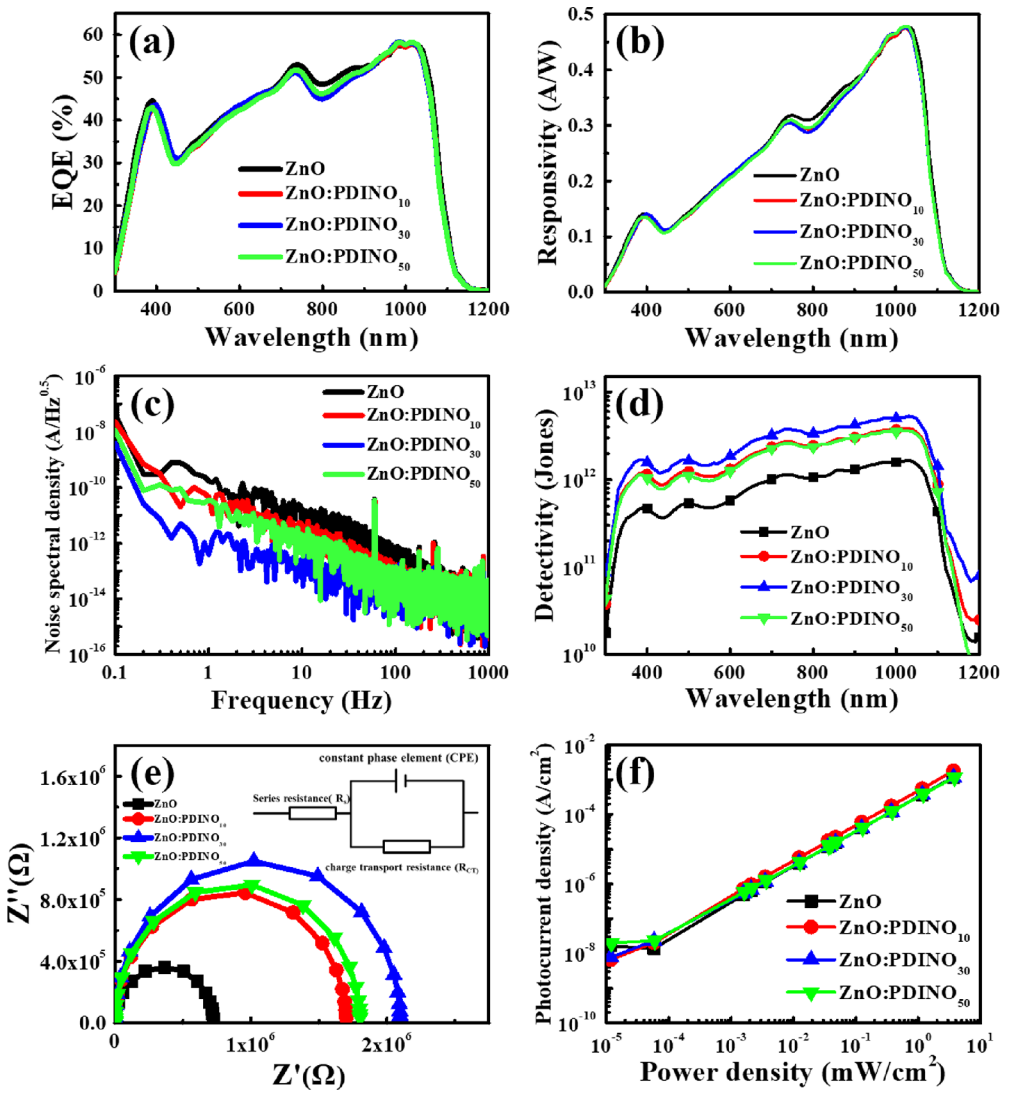

Figure 3. (a) EQE spectrum, (b) responsivity spectrum, (c) noise spectral density, (d) detectivity spectrum, (e) Nyquist plots, and (f) LDR measurements of OPDs with ZnO:PDINO hybrid ETLs at varying ratios of 0, 10, 30, and 50 vol % of PDINO. EQE and responsivity are obtained at 300−1000 nm wavelength under −1 V bias. The inset in (e) shows the corresponding RC circuit diagram of the system.

that blending PDINO in ZnO can effectively reduce the J_D with the best result obtained under the condition of 30 vol % (ZnO:PDINO$_{30}$). The J_D at −1 V can be reduced from 2.1×10^{-7} to 2.1×10^{-8} A/cm^2, which can be attributed to the shift of the work function of the ZnO thin film by adding PDINO (Figure S1). Figure 2b shows the SCLC measurements to quantify the defect density in the OPD with ZnO:PDINO hybrid ETL. An electron-only device was fabricated for this measurement. It is noteworthy that the double logarithmic forward bias J−V reveals the power-law behavior of $J \sim V^n$, where n denotes the slope of each region. The n value varies with the injection level and is linked with the distribution of trapping centers. The region of $n \sim 1$ reflects the ohmic region, $n \sim 2$ is the SCLC region, and $n > 2$ represents the trap-limited region.[36,37] Here, the corresponding SCLC curve of the ZnO:PDINO blend demonstrates three visible curves. The J_D−V curve characterized in SCLC can be described by[38,39]

$$J = \frac{9}{8}\varepsilon\mu\frac{(V - V_{BI})^2}{L^3} \quad (1)$$

where J represents the current density, ε represents the dielectric constant, μ represents the carrier mobility, V

https://doi.org/10.1021/acsami.4c01466
ACS Appl. Mater. Interfaces 2024, 16, 27576−27586

Table 2. Values of EQE, R, D^*, D_n^*, and LDR of OPDs with ZnO:PDINO Hybrid ETLs at Varying Ratios of 0, 10, 30, and 50 vol% of PDINO

ETL[a]	EQE[b] (%)	responsivity (A/W)	D^*(Jones)	D_n^*(Jones)	LDR (dB)
ZnO	57.2 (57.1 ± 0.1)	0.46	1.57×10^{12}	3.26×10^{11}	75
ZnO:PDINO$_{10}$	57.1 (56.8 ± 0.3)	0.46	3.54×10^{12}	6.05×10^{11}	94
ZnO:PDINO$_{30}$	57.7 (57.5 ± 0.2)	0.47	4.99×10^{12}	1.09×10^{12}	95
ZnO:PDINO$_{50}$	57.6 (57.4 ± 0.2)	0.47	3.92×10^{12}	8.48×10^{11}	90

[a]The average data are obtained from 10 devices for each ETL. [b]EQE and responsivity values were obtained at a wavelength of 1000 nm under −1 V bias.

represents applied voltage, V_{BI} represents built-in voltage, and L represents the thickness of the organic layer. From eq 2, the trap density (N_t) can be expressed by[38]

$$V_{TFL} = \frac{qN_tL^2}{2\varepsilon} \tag{2}$$

where V_{TFL} represents the trap-filled-limited voltage curve and q represents the elementary charge particle. Following this, the SCLC curve demonstrates that PDINO can effectively reduce the defect density and increase electron mobility, as shown in Figure 2c. Furthermore, the SCLC curve of the device with PEIE demonstrates a spatial constraint that is significantly lower than PDINO (Figure S2). All obtained values of J_D, μ_e, V_{TFL}, and N_t of OPD with different ZnO:PDINO ETL are shown in Table 1. These results demonstrate that PDINO can effectively reduce the J_D and improve charge transfer. To elucidate the effect of PDINO hybrid with ZnO on its surface morphologies, AFM measurements are obtained, as shown in Figure S3. It was found that the photoactive layer deposited on various ZnO:PDINO ETLs at hybrid ratios of 0, 10, 30, and 50 vol % of PDINO demonstrates a roughness of 1.7, 1.6, 1.65, and 1.55 mm, respectively. The minimal decrease in the surface roughness of the active layer with ZnO:PDINO hybrid ETL suggests that the passivation of defects on the surface of the ZnO may influence variations in J_D and responsivity.

To further analyze the effect of PDINO on the performance of ZnO:PDINO hybrid ETL-based OPD, the absorption behavior and the bandgap energy of the active layer (PTB7-Th and COTIC-4F) were initially measured using the UV−vis absorption spectra (Figure S4). The main regions of the absorption for PTB7-Th and COTIC-4F were 400−800 and 600−1200 nm, respectively. The complementary absorption behavior of these two materials enabled the response range of PTB7-Th:COTIC-4F blends to cover wavelengths from the visible to the NIR. The EQE, representing the charge generation and collection ability of the OPD, is also observed in Figure 3a. The EQE can be well explained by eq 3:[40]

$$\mathrm{EQE} = \frac{\chi\tau}{T} = \frac{\chi\tau\mu V}{L^2} \tag{3}$$

where χ represents the fraction of dissociated excitons, τ represents the lifetime of trapped electrons, T is the hole transport time, μ represents carrier mobility, V is the applied bias, and L represents the active layer thickness. Here, no significant EQE deterioration was observed, and the EQE was still as high as 57% at a wavelength of 1000 nm. Also, OPDs with an increased amount of PDINO exhibited a slight increase in the EQE. Figure 3b displays the responsivity of the OPD, illustrating the ratio of the optical power of the material to the collected current under illumination. The responsivity can be calculated by eq 4:[20,28]

$$R\left(\frac{A}{W}\right) = \frac{\mathrm{EQE} \times q \times \lambda}{hc} = \frac{\mathrm{EQE}}{100\%} \times \frac{\lambda}{1240(\mathrm{nm}^{W}/_{A})} \tag{4}$$

where R represents the responsivity, q represents the electric charge, and λ represents the incident light wavelength. For OPDs, the specific detectivity (D^*) describes the ability of OPD to sense light, and this performance mainly depends on the J_D and light response. The calculation for D^* of the material following J_D is expressed by the following requation:[7,18]

$$D^* = \frac{R(\lambda)}{\sqrt{2 \times q \times J_D}} \tag{5}$$

However, this definition only includes J_D as the source of noise, leading to inaccuracies in D^* calculations with overestimated results.[18] By utilizing white noise for calculation, the equation for D_n^* is determined as follows:[8,18]

$$D_n^* = \frac{R\sqrt{A\Delta f}}{i_n} \tag{6}$$

where A represents the active area of the OPD, Δf represents the measurement system bandwidth, and i_n represents the white noise. The calculated responsivity of the OPD displays a slight increase with an increase in PDINO. Figure 3c demonstrates the i_n−frequency (N−F) curve of the OPD with varying PDINO hybrid blending. According to the literature,[11] i_n occurs in an interval that has nothing to do with frequency; thus, the i_n between 100 and 1000 Hz as the source of i_n was utilized. In the hybrid ETL, the devices based on ZnO:PDINO$_{30}$ achieved the lowest i_n of 2.4×10^{-14} A/Hz. Figure 3d shows the D^* of the OPDs with varying ZnO:PDINO ETLs. Here, the ZnO:PDINO$_{30}$ device demonstrates the highest D^*; however, a further increase of up to 50 vol % of PDINO shows an evident decrease in the D^*. The overall performances of the OPDs with ZnO:PDINO ETLs of varying PDINO ratios are displayed in Table 2.

Moreover, we conducted EIS to precisely investigate the effects of hybrid PDINO on the interfacial resistance and charge behavior of the OPDs. Figure 3e shows the Nyquist plots of the OPDs with ZnO:PDINO ETLs. According to the literature, the semicircle arc at high frequencies (left-hand side) can be attributed to the charge transport behavior whereas the semicircle arc at low frequencies (right-hand side) is connected to the charge recombination process.[41,42] Also, the semicircle diameter extending on the real axis represents the influence of R_{CT}, where higher R_{CT} leads to a reduction of J_D.[41,42] As shown in the inset of Figure 3e, the OPD can be represented by an equivalent circuit consisting of an internal series resistance (R_S), a charge transport resistance (R_{CT}), and a constant phase element (CPE). The OPD device based on ZnO:PDINO$_{30}$ ETL exhibits higher R_{CT} compared to other

https://doi.org/10.1021/acsami.4c01466
ACS Appl. Mater. Interfaces 2024, 16, 27576−27586

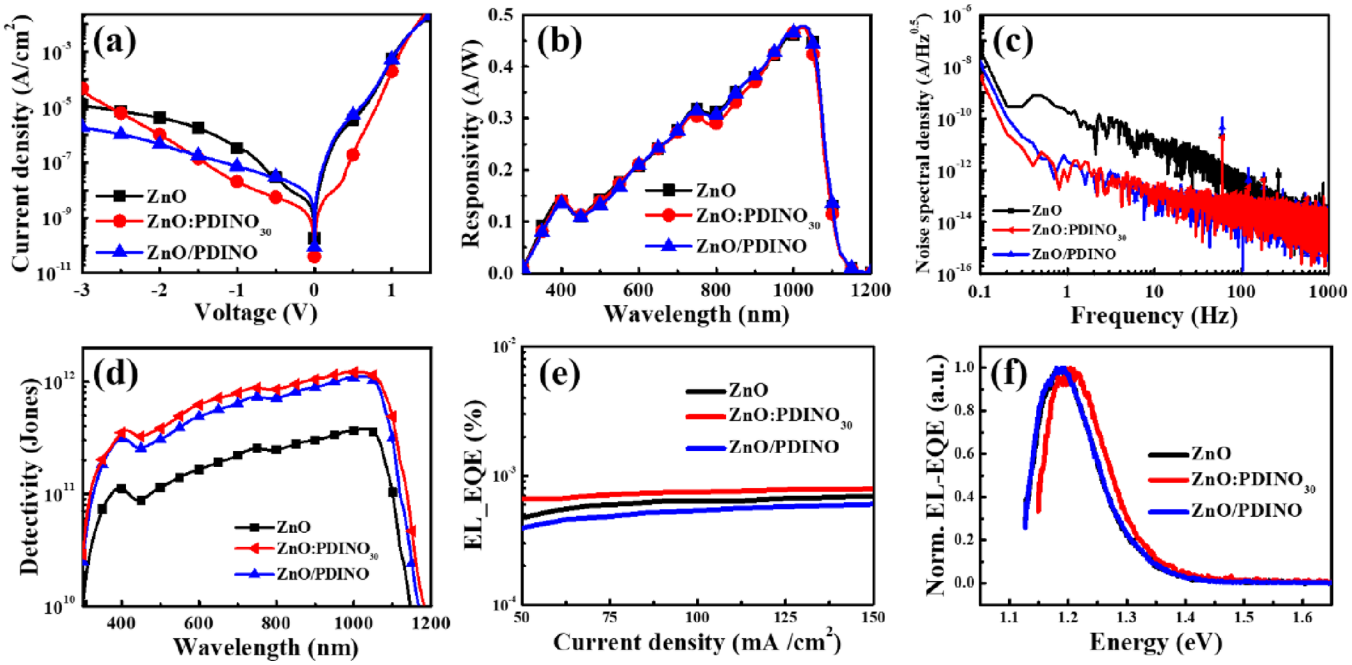

Figure 4. (a) J_D−V curves, (b) Responsivity, (c) N−F curve, (d) detectivity, and (e, f) EL_{EQE} spectra of the OPDs with ZnO, ZnO:PDINO$_{30}$ (hybrid), and ZnO/PDINO (bilayer) ETLs.

OPDs, indicating that the ZnO:PDINO$_{30}$ ETL-based OPDs have better interfacial contact and charge transport behavior. The increase in R_{CT} suggests that PDINO can effectively assist in the reduction of leakage current and J_D, resulting in high responsivity of the OPDs. Figure 3f shows the photocurrent density as a function of light intensity of the OPD characterized by the LDR. The LDR measurement was recorded under 940 nm light with modulated power light intensities at 1 mW. The OPDs fabricated from ZnO:PDINO$_{30}$ exhibit the highest LDR of 95 dB, indicating that OPDs can detect light within the largest light intensity range. Figure S5 shows the fitted relationship between LDR and J_D. It can be observed that the measured minimum photocurrent and J_D are very close to each other. This result also implies that the ETL of ZnO:PDINO$_{30}$ exhibits low trap density. Based on the above results, we have improved the charge transport and defect passivation at the interface between the transparent electrode and the active layer by blending ZnO and PDINO as the ETL for OPDs, proving that PDINO is a promising cathode interlayer.

To further verify the generalization of PDINO as a cathode interlayer, we fabricated the OPDs with the commonly used bilayer structured ETL (ZnO/PDINO) and compared the performance. Figure 4a illustrates the effect of ZnO/PDINO ETL on the J_D of OPDs. In comparison to OPDs with 0 vol % of PDINO, OPDs with bilayer ETL showed a reduced J_D from 2.1×10^{-7} to 6.1×10^{-8} A/cm^2 at −1 V. This result suggests that the deposition of PDINO on the ZnO layer reduce J_D, implying that PDINO can fill the surface defects. However, compared with the OPDs fabricated from hybrid ETL (Table 1), the bilayer-ETL-based OPDs are less effective in suppressing the generated current leakage. This means that internal defects cannot be filled by the bilayer structure, which makes the J_D susceptible to increase due to the charge tunneling caused by internal defects. Figure 4b shows the responsivity spectrum of the OPD devices with these ETLs. NIR-OPDs based on the pristine ZnO and bilayer ETL demonstrated the same responsivity of 0.46 A/W, while hybrid ETL demonstrated a responsivity of 0.47 A/W at a wavelength of 1000 nm. The nearly identical responsivities indicate that the EQE in the systems mainly depends on the selection of the active layer materials, on which the ETL has little influence on the overall EQE of OPDs. Figure 4c shows the N−F curves of the OPDs with ZnO, ZnO:PDINO, and ZnO/PDINO ETLs. The noise current of OPDs with PDINO, either bilayer or hybrid structured ETLs, is significantly lower than that of OPDs with pristine ZnO, which means that the introduction of PDINO can improve the overall defects in ZnO. Finally, the detectivity of the OPDs fabricated from ZnO, bilayer, and hybrid ETLs illustrates that the addition of PDINO in either way can substantially increase the detectivity, as shown in Figure 4d. Among them, the hybrid ETL-based OPD with the highest detectivity measuring 1.09×10^{12} Jones at −1 V and 1000 nm wavelength. These results demonstrate that PDINO is a promising cathode interlayer, which can be used to reduce J_D and improve the responsivity and detectivity of the OPD devices efficiently. To elucidate the difference in the performance of the OPD device with ZnO:PDINO and ZnO/PDINO ETLs, the change of energy loss was investigated using FTPS-EQE and electroluminescence of quantum efficiency (EL_{EQE}).[43,44] Figure S6 displays the characteristic values of charge transfer state energy (E_{CT}) of the active layer with various ETL systems with PDINO. Here, E_{CT} demonstrated indistinct values for various ETL systems. The insignificant change observed in E_{CT} is suggested by the little effect of the modulation of ETL on the state energy in the active layer material. However, it can be observed that the hybrid ETL-based OPD displays a higher EL_{EQE} of 7.83×10^{-4} than the bilayer and ZnO ETL-based OPD (Figure 4e). This increase in EL_{EQE} correlates with a decrease in energy loss.[45−47] In addition, a significant energy shift in the bilayer ETL-based OPDs can be observed in the normalized EL_{EQE} spectra (Figure 4f), which may have contributed to the energy loss in the bilayer ETL-based OPD devices. Our direct comparative

https://doi.org/10.1021/acsami.4c01466
ACS Appl. Mater. Interfaces 2024, 16, 27576−27586

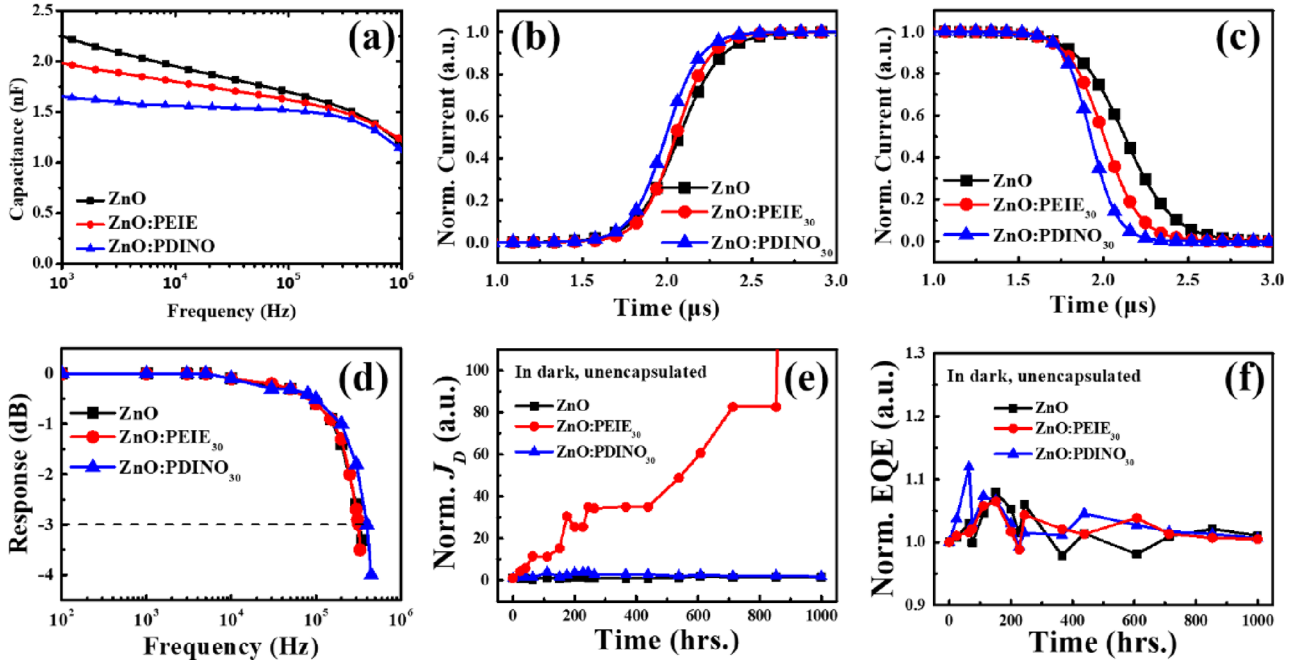

Figure 5. (a) $C-F$ plots, (b) rise time, (c) fall time, (d) cutoff frequencies, (e) J_D, and (f) EQE stability of the OPDs with ZnO, ZnO:PDINO$_{30}$ hybrid, and ZnO:PEIE$_{30}$ hybrid bilayer ETLs.

analyses of ETL for two-step (bilayer) and one-step (hybrid) deposit processes reveal the effectiveness of PDINO in both ETL structures. Notably, our results indicate that the hybrid ETL not only offers enhanced process convenience but also demonstrates superior performance in defect passivation, charge-transport behavior, and energy loss, leading to notable improvement of OPDs.

To further demonstrate the superiority of our ZnO:PDINO hybrid ETL on the OPD devices, commonly used PEIE was also blended with the ZnO in hybrid and bilayer structures. As shown in Figure S7, OPDs with PEIE-hybrid ETLs demonstrated higher performance than OPDs with PEIE-bilayer ETLs, which is consistent with the OPDs with PDINO-based ETLs. The J_D of the OPDs with ETLs of ZnO, ZnO:PEIE, and ZnO:PDINO are compared (Figure 3a) and Figure S7a), where ZnO:PDINO-based OPD demonstrated a significant J_D drop as compared to ZnO:PEIE-based OPD. The $N-F$ curve demonstrates a comparable lower i_n in ZnO:PEIE and ZnO:PDINO hybrid ETL-based OPDs than that of ZnO ETL-based OPDs, which is attributed to the significant effects of the hybrid system in efficiently filling the overall defects, interfacial and internal defects in ZnO, as shown in Figure 3c and Figure S7d. Also, ZnO:PEIE-hybrid ETL-based OPD demonstrates an increased D_n* (Figure S7e) and R_{CT} (Figure S7f). Figure S6 displays the SCLC results of PEIE-based OPDs, demonstrating the electron mobility and trap density of the OPDs fabricated from PEIE-hybrid ETLs with various PEIE amounts. We found that the electron mobility and trap density of the PEIE-hybrid-based OPDs are about one order of magnitude lower than those of the PDINO-hybrid-based OPDs, regardless of the PEIE−hybrid ratio, which is attributed to the high electron mobility of PDINO. The observed overall enhancements found in ZnO:PEIE$_{30}$ display less effectivity than ZnO:PDINO$_{30}$, which is attributed to the insulating property of PEIE, which reduces the efficiency of charge collection.

Figure 5a is the capacitance-frequency ($C-F$) plots of the OPDs with ETLs of ZnO:PEIE and ZnO:PDINO, where the impedance response in low and intermediate frequency regions is attributed to the charge dynamic processes at the ETL/active layers interface.[48] As the forward bias is applied under dark, the inner charge dynamics can be treated as an electron back transfer process where electrons are injected from the external circuit to ETL and then pass through the ETL/active layer interface and then to the BHJ just opposite to the flowing direction in operation. The larger capacitance of the ZnO ETL-based device implies a more serious interfacial charge accumulation indicative of large electron transfer resistance. Upon introduction of PEIE and PDINO in hybrid systems with ZnO ETL, the device demonstrates lower $C-F$ plots. Hybrid ETL OPD displays a significant reduction of the capacitance indicating that the hybrid ETL system can respond more effectively to higher frequencies of incident light. The hybrid ETL with PDINO demonstrates a lower $C-F$ plot than that of PEIE, which may have originated from the lower dielectric constants and/or lower electronic polarizability of PDINO that can result in lower capacitance. Subsequently, we study the response speed of the OPD with ZnO and hybrid ETLs to the light signal and investigate its transient response time. OPDs are generally operated under reverse bias voltage, which improves the charge extraction behavior of the devices.[48,49] Response speed defines the charge transfer capability of the photoelectric detecting element under transient light, which is represented by rise time and fall time, respectively.[10] The rise time is affected by the charge collection ability, and the fall time is affected by the charge output.[50,51] Figure 5b and c shows the rise and fall times, respectively, of the OPDs with ZnO and hybrid ETLs. Under light with a wavelength of 940 nm, the ZnO:PDINO$_{30}$ ETL-based OPD demonstrates the fastest rising speed of 410 ns, which is attributed to the good conductivity of PDINO. This, in turn, improves the ability of charge collection, while the falling time of the ZnO:PDINO$_{30}$ ETL-based OPD also

https://doi.org/10.1021/acsami.4c01466
ACS Appl. Mater. Interfaces 2024, 16, 27576−27586

reaches a maximum of 330 ns. The fast charge output capability of the ZnO:$PDINO_{30}$ ETL-based OPD is attributed to the hybrid method reducing the overall defect in ZnO, thus improving the performance of charge transfer. As demonstrated by ZnO:PEIE, the charge transport performance is also significantly improved; however, the charge collection and output ability of PEIE is slightly lower than that of PDINO, which is attributed to the insulating characteristics of PEIE. We also measured the response rate of ZnO:PEIE ETL with varying ratios of PEIE, as shown in Figure S8. The resultant response speeds of these components are proportional to the mobility, indicating that high electron mobility can increase the response speed of the components. In addition, we deeply explored the response limit of the OPD with ZnO, ZnO:$PEIE_{30}$, and ZnO:$PDINO_{30}$ hybrid ETLs to NIR light, where the cutoff frequency of the samples was observed. The cutoff frequency (f_{-3dB}) defines the light frequency of the OPD at −3 dB, which is mainly related to the charge transfer time and series resistance of the material, as shown in Figure 5d. Due to the high conductivity of PDINO, the time of charge transfer is improved, thereby improving the cutoff frequency of the OPD. All obtained values of the rise time, fall time, and f_{-3dB} of the OPD with ZnO, ZnO:$PEIE_{30}$, and ZnO:$PDINO_{30}$ are listed in Table 3.

Table 3. Calculated Values of Rise Time, Fall Time, and f_{-3dB} of OPD with ZnO, ZnO:$PEIE_{30}$, and ZnO:$PDINO_{30}$ Hybrid ETL

ETL[a]	rise time (ns)	fall time (ns)	f_{-3dB}(kHz)
ZnO	530	600	310
ZnO:$PEIE_{30}$	450	480	320
ZnO:$PDINO_{30}$	410	330	400

[a]The data are obtained from best devices for each ETL.

Finally, we investigated the stability of the ZnO:$PDINO_{30}$ hybrid ETL OPD. Figure 5e displays the J_D stability of the unencapsulated OPDs with various ETLs under dark storage. It was found that the OPDs with ZnO:$PDINO_{30}$ ETL maintained consistent J_D levels even after exposure to ambient environment for 1000 h. In contrast, the OPD with ZnO:$PEIE_{30}$ ETL demonstrates a significant increase in J_D after 1000 h of exposure in an ambient environment. This is attributed to the amine group in PEIE, which destroys the structure of nonfullerene materials in ambient conditions.[29] We evaluated the J_D stability of the device, as well as the photocurrent stability under 530 and 1000 nm illumination for 10 days (Figure S9). From Figure S9, we observed that the photocurrents of the devices fabricated from the three ETLs show a slight variation under reverse bias after 10 days of illumination, which indicates that the photocurrent stability of the devices is good. However, in terms of J_D stability, the J_D of the devices based on ZnO:PEIE ETL increases significantly compared to the other two devices after 10 days of storage in a dry cabinet (~25 °C and 50%RH). This result suggests that the addition of PEIE does destabilize the J_D of the OPDs. In addition, we also simulated the actual operation of OPDs at different light intensities and frequencies using a 940 nm laser, by which we evaluated the change in response speed of the OPDs after 10 days of storage, as shown in Figure S10. The results show that there is no obvious change in the response speeds of the three devices at 1 kHz and 10 kHz, but at the high frequency of 100 kHz, the response speeds of these devices exhibit a significant difference. At high frequency (100 kHz) and low light intensity (10 μW), the ZnO-based OPDs reveal a reducing response speed, which is due to the high intrinsic J_D of the devices. On the other hand, although the J_D of the ZnO:PEIE-based devices has been improved, the devices still exhibit slower response speeds under this condition, which

Table 4. List of Recent State-of-the-Art Reports on High-Performance NIR-OPD

year[a]	active layer	spectral region (nm)	J_d (A/cm^2)	−3 dB/τr, τf	R (A/W)	maximum D^*[a] (Jones)
this work	PTB7-Th:COTIC-4F	300−1100	2.1×10^{-8} @−1 V	400 kHz 400/320 (ns)	0.46 1000 nm @−1 V	5.0×10^{12} (based on J_d) @1000 nm 1.1×10^{12} (based on S_n)
this work @ 0.1 V	PTB7-Th:COTIC-4F	300−1100	1.4×10^{-9} @0.1 V		0.44 @1000 nm @−0.1 V	2.0×10^{13} (based on J_d) @1000 nm
2021[16]	PTB7-Th:COTIC-4Cl: $PC_{71}BM$	300−1200	1.1×10^{-8} @−0.1 V	1 MHz 780/940 (ns)	0.35 @1060 nm @−0.1 V	5.9×10^{12}@1060 nm (based on J_d)
2021[14]	PTB7-Th:COTIC-4F	400−1050	5.0×10^{-9} @−2 V		0.25 A/W @1050 nm @−2 V	6.0×10^{12} @1050 nm (based on J_d)
2022[15]	PTB7-Th:COTIC-4F	400−1100	8.5×10^{-7} @−1 V	21/24 (μs)	0.42 A/W @1000 nm @−1 V	7.95×10^{11} @940 nm (based on J_d)
2022[22]	PTB7-Th:COTIC-4F: Y6	400−1100	1.2×10^{-9} @−0.1 V	45 kHz 13.6/12.5 (μs)	0.41 A/W @1060 nm @−0.1 V	2.10×10^{13} @940 nm (based on J_d)
2022[52]	PTB7-Th:COTIC-4F: Y6	400−1070	5.61×10^{-10} @−0.1 V	60 kHz	0.45 A/W @1050 nm @−0.1 V	7.13×10^{12} @1050 nm (based on S_n)
2022[53]	PD004:PD-A2	350−1100	8.60×10^{-8} @−8 V	350 Hz 0.45 (ms)	0.46 A/W @1080 nm @−8 V	2.34×10^{12} (based on J_d) @1080 nm 1.7×10^{10} (based on S_n)
2023[54]	PTB7-Th:COTCN2	300−1200	1.08×10^{-7} @−0.5 V	61.5 kHz	0.23 A/W @1000 nm @−0.5 V	1.18×10^{12} (based on J_d) @1080 nm 1.33×10^{11} (based on S_n)
2023[55]	PTB7-Th:COB	300−1100	5.22×10^{-8} @−0.5 V	52.1 kHz	0.455 A/W @970 nm @−0.5 V	3.29×10^{12} @970 nm (based on S_n)
2023[56]	PTB7-Th:YOR1	300−1000	1.58×10^{-10} @−0.1 V		0.141 A/W @950 nm @−0.1 V	1.98×10^{13} (based on J_d) @950 nm 1.29×10^{12} (based on S_n)
2023[57]	PCE10:BTPV-4F-eC9	360−1050	4.65×10^{-10} @0 V	>100 kHz 8/7.6 (μs)	0.14 A/W @1030 nm @0 V	1.14×10^{13} (based on J_d) @1080 nm 2.0×10^{12} (based on S_n)
2024[58]	PTB7-Th:COTIC-4F	350−1100	2.30×10^{-8} @−1 V		0.339 A/W @1000 nm @−1 V	3.9×10^{12} @1000 nm (based on J_d)

[a]The references from the list were reported between the years 2021 and 2024.

https://doi.org/10.1021/acsami.4c01466
ACS Appl. Mater. Interfaces 2024, 16, 27576−27586

suggests that more internal traps lead to a prolonged charge-filling time. The ZnO:PDINO-based OPDs exhibit stable response speeds, indicating that the ZnO:PDINO layer is still an excellent ETL for OPDs even at high frequency with low light intensity. Additionally, the EQE stability of ZnO:PDINO$_{30}$ hybrid ETL OPD at a wavelength of 1000 nm is shown in Figure 5f. After 1000 h of storage in an ambient environment, no significant decrease in the EQE was found, indicating that the charge extraction of aging devices is the same as as-cast devices. The above investigations imply that ZnO:PDINO$_{30}$ hybrid ETL can not only effectively optimize the performance of the OPDs but also possess high stability in ambient conditions. Our overall performance analyses of OPD with PDINO as a hybrid blend in ETL indicate that PDINO significantly contributes as a cathode interlayer. For comparison of our results,[52−58] Table 4 provides a list of the recent state-of-the-art reports on high-performance NIR-OPD while Figure S11 provides a summary of the specific detectivity (D_n*) of NIR-OPDs at similar wavelengths. Notably, our OPDs fabricated from ZnO:PDINO hybrid ETL exhibit the highest D_n* under the same operating conditions in the PTB7-COTIC-4F system. In addition, NIR-OPDs are commonly fabricated from glass/ITO substrates, but the reflectance and transmittance of ITO in the NIR region (especially over 1000 nm) increased significantly (more than 20%), which is one of the reasons for the low EQE.[59] Some research groups have demonstrated promising alternative electrodes that maintain good electrical and high transmittance in the NIR region.[60,61] These electrodes are expected to contribute to the improvement of the EQE and responsivity of the NIR-OPDs.

4. CONCLUSIONS

In this study, we systematically investigated the impact of PDINO blended in a hybrid system with ZnO ETL on modulating J_D for OPDs. Employing PDINO in hybrid systems led to an outstanding drop in J_D to 2.1×10^{-8} A/cm^2 at −1 V, coupled with a remarkably high responsivity of 0.47 A/W at a 1000 nm wavelength. This reduction in J_D also resulted in a notably enhanced detectivity of 1.09×10^{12} Jones. Also, the effects of PDINO in hybrid and bilayer ETL systems were thoroughly studied. Here, the PDINO in both systems participated in the enhancement of the OPD; however, the hybrid system is suggested to effectively restrain J_D generation than the bilayer system by efficiently filling oxygen vacancies within and on the surface of the ZnO film layer, thereby reducing injection current due to charge tunneling. Furthermore, the effectiveness of PDINO as a blend in ETL versus the commonly used PEIE was investigated. In comparison to PEIE, PDINO revealed a significant improvement in the R_{CT} of the OPD, indicating enhanced charge transport between interfaces. Also, the high conductivity of PDINO with ZnO ETL assisted in the reduction of capacitance, which effectively lowers the interfacial charge accumulation that leads to charge transfer resistance. These improvements were also evident in the transient response speed results, with a rise time of 410 ns and a fall time of 330 ns achieved under illumination with a 940 nm wavelength light source at −1 V. These results demonstrate the efficient charge collection and transport capabilities in the ZnO:PDINO hybrid ETL-based OPD. Finally, the excellent compatibility of PDINO with non-fullerene materials demonstrated prolonged highly stable EQE for an impressive 1000 h at room temperature without the need for packaging. This research provides valuable insights into the optimization of ETL for OPDs, offering a promising avenue for the development of highly efficient, stable, and sensitive PDs for a wide array of applications.

ASSOCIATED CONTENT

Supporting Information

The Supporting Information is available free of charge at https://pubs.acs.org/doi/10.1021/acsami.4c01466.

Work function of OPDs, SCLC and calculated electron mobilities of electron-only OPDs, AFM images of ETLs, absorption spectra of films, LDR fittings, FTPS_EQE spectra of OPDs, performance of OPDs, rise time and fall time of OPDs, stability measurements of OPDs, and advances in performance of OPDs reported in the latest literature (PDF)

AUTHOR INFORMATION

Corresponding Author

Yu-Ching Huang − *Department of Materials Engineering, Ming Chi University of Technology, New Taipei City 24301, Taiwan; Organic Electronics Research Center and Biochemical Technology R&D Center, Ming Chi University of Technology, New Taipei City 24301, Taiwan; Department of Chemical and Materials Engineering, Chang Gung University, Taoyuan 33302, Taiwan;* orcid.org/0000-0003-4772-8050; Email: huangyc@mail.mcut.edu.tw

Authors

Tai-Yuan Wang − *Department of Materials Engineering, Ming Chi University of Technology, New Taipei City 24301, Taiwan*

Zhi-Hao Huang − *Department of Materials Engineering, Ming Chi University of Technology, New Taipei City 24301, Taiwan; Department of Chemical and Materials Engineering, Chang Gung University, Taoyuan 33302, Taiwan*

Svette Reina Merden Solante Santiago − *Department of Materials Engineering, Ming Chi University of Technology, New Taipei City 24301, Taiwan;* orcid.org/0009-0004-3367-7859

Complete contact information is available at: https://pubs.acs.org/10.1021/acsami.4c01466

Author Contributions

Y.-C.H. conceptualized and finalized this manuscript and secured the financial funds for the research. T.-Y.W. conducted the experiments and collected the data. Z.-H.H. and S.R.M.S.S. evaluated and finalized the data and wrote the manuscript.

Notes

The authors declare no competing financial interest.

ACKNOWLEDGMENTS

This research was supported in full by the National Science and Technology Council of Taiwan (Grant numbers: NSTC 112-2622-E-131-011, NSTC 112-2628-E-131-001-MY4, NSTC 111-2221-E-131-022).

REFERENCES

(1) Jacoutot, P.; Scaccabarozzi, A. D.; Zhang, T.; Qiao, Z.; Aniés, F.; Neophytou, M.; Bristow, H.; Kumar, R.; Moser, M.; Nega, A. D.; Schiza, A.; Dimitrakopoulou-Strauss, A.; Gregoriou, V. G.; Anthopoulos, T. D.; Heeney, M.; McCulloch, I.; Bakulin, A. A.; Chochos, C. L.; Gasparini, N. Infrared Organic Photodetectors

Employing Ultralow Bandgap Polymer and Non-Fullerene Acceptors for Biometric Monitoring. *Small* **2022**, *18* (15), No. 2200580.
(2) Kim, J. H.; Liess, A.; Stolte, M.; Krause, A.-M.; Stepanenko, V.; Zhong, C.; Bialas, D.; Spano, F.; Würthner, F. An Efficient Narrowband Near-Infrared at 1040 nm Organic Photodetector Realized by Intermolecular Charge Transfer Mediated Coupling Based on a Squaraine Dye. *Adv. Mater.* **2021**, *33* (26), No. 2100582.
(3) Geum, D.-M.; Kim, S.; Kim, S. K.; Kang, S.; Kyhm, J.; Song, J.; Choi, W. J.; Yoon, E. Monolithic integration of visible GaAs and near-infrared InGaAs for multicolor photodetectors by using high-throughput epitaxial lift-off toward high-resolution imaging systems. *Sci. Rep.* **2019**, *9* (1), 18661.
(4) Pejović, V.; Georgitzikis, E.; Lieberman, I.; Malinowski, P. E.; Heremans, P.; Cheyns, D. Photodetectors Based on Lead Sulfide Quantum Dot and Organic Absorbers for Multispectral Sensing in the Visible to Short-Wave Infrared Range. *Adv. Funct. Mater.* **2022**, *32* (28), No. 2201424.
(5) Shi, L.; Chen, K.; Zhai, A.; Li, G.; Fan, M.; Hao, Y.; Zhu, F.; Zhang, H.; Cui, Y. Status and Outlook of Metal−Inorganic Semiconductor−Metal Photodetectors. *Laser Photonics Rev.* **2021**, *15* (1), No. 2000401.
(6) Ren, H.; Chen, J.-D.; Li, Y.-Q.; Tang, J.-X. Recent Progress in Organic Photodetectors and their Applications. *Adv. Sci.* **2021**, *8* (1), No. 2002418.
(7) Huang, J.; Lee, J.; Vollbrecht, J.; Brus, V. V.; Dixon, A. L.; Cao, D. X.; Zhu, Z.; Du, Z.; Wang, H.; Cho, K.; Bazan, G. C.; Nguyen, T.-Q. A High-Performance Solution-Processed Organic Photodetector for Near-Infrared Sensing. *Adv. Mater.* **2020**, *32* (1), No. 1906027.
(8) Zhao, Z.; Xu, C.; Niu, L.; Zhang, X.; Zhang, F. Recent Progress on Broadband Organic Photodetectors and their Applications. *Laser Photonics Rev.* **2020**, *14* (11), No. 2000262.
(9) Huang, Z.; Zhong, Z.; Peng, F.; Ying, L.; Yu, G.; Huang, F.; Cao, Y. Copper Thiocyanate as an Anode Interfacial Layer for Efficient Near-Infrared Organic Photodetector. *ACS Appl. Mater. Interfaces* **2021**, *13* (1), 1027−1034.
(10) Kuo, K.-H.; Estrada, R.; Lee, C.-C.; Al Amin, N. R.; Li, Y.-Z.; Hadiyanto, M. Y.; Liu, S.-W.; Wong, K.-T. A New Dioxasilepine−Aryldiamine Hybrid Electron-Blocking Material for Wide Linear Dynamic Range and Fast Response Organic Photodetector. *ACS Appl. Mater. Interfaces* **2022**, *14* (16), 18782−18793.
(11) Lee, C.-C.; Estrada, R.; Li, Y.-Z.; Biring, S.; Amin, N. R. A.; Li, M.-Z.; Liu, S.-W.; Wong, K.-T. Vacuum-Processed Small Molecule Organic Photodetectors with Low Dark Current Density and Strong Response to Near-Infrared Wavelength. *Adv. Opt. Mater.* **2020**, *8* (17), No. 2000519.
(12) Lee, J.; Ko, S.-J.; Lee, H.; Huang, J.; Zhu, Z.; Seifrid, M.; Vollbrecht, J.; Brus, V. V.; Karki, A.; Wang, H.; Cho, K.; Nguyen, T.-Q.; Bazan, G. C. Side-Chain Engineering of nonfullerene Acceptors for Near-Infrared Organic Photodetectors and Photovoltaics. *ACS Energy Lett.* **2019**, *4* (6), 1401−1409.
(13) Li, J.; Liu, G.; Liu, W.; Si, Y.; Deng, W.; Wu, H. Highly Sensitive UV−Vis-to-Near-Infrared Organic Photodetectors Employing ZnO: Polyethylenimine ethoxylated Composite as Hole-Blocking Layer. *Adv. Photonics Res.* **2022**, *3* (4), No. 2100269.
(14) Yang, W.; Qiu, W.; Georgitzikis, E.; Simoen, E.; Serron, J.; Lee, J.; Lieberman, I.; Cheyns, D.; Malinowski, P.; Genoe, J.; Chen, H.; Heremans, P. Mitigating Dark Current for High-Performance Near-Infrared Organic Photodiodes via Charge Blocking and Defect Passivation. *ACS Appl. Mater. Interfaces* **2021**, *13* (14), 16766−16774.
(15) Simões, J.; Dong, T.; Yang, Z. Non-Fullerene Acceptor Organic Photodetector for Skin-Conformable Photoplethysmography Applications. *Adv. Mater. Interfaces* **2022**, *9* (10), No. 2101897.
(16) Zhong, Z.; Peng, F.; Ying, L.; Yu, G.; Huang, F.; Cao, Y. Ternary organic photodiodes with spectral response from 300 to 1200 nm for spectrometer application. *Sci. China Mater.* **2021**, *64* (10), 2430−2438.
(17) Wu, S.; Xiao, B.; Zhao, B.; He, Z.; Wu, H.; Cao, Y. High Sensitivity Polymer Visible-Near Infrared Photodetectors via an Inverted Device Structure and Manipulation of Injection Barrier Height. *Small* **2016**, *12* (25), 3374−3380.
(18) Huang, Y.-C.; Huang, Z.-H.; Wang, T.-Y.; Chaudhary, P.; Hsu, J.-F.; Lee, K.-M. A promising non-fullerene acceptor for near-infrared organic photodetectors operating with low dark current and high response speed. *Chem. Eng. J.* **2023**, *464*, No. 142633.
(19) Kublitski, J.; Hofacker, A.; Boroujeni, B. K.; Benduhn, J.; Nikolis, V. C.; Kaiser, C.; Spoltore, D.; Kleemann, H.; Fischer, A.; Ellinger, F.; Vandewal, K.; Leo, K. Reverse dark current in organic photodetectors and the major role of traps as source of noise. *Nat. Commun.* **2021**, *12* (1), 551.
(20) Joseph, A.; Pillai, A. B.; Pulikodan, V. K.; Alexander, A.; Muhammed, R.; Namboothiry, M. A. G. Solution-Processed Self-Powered Panchromatic Organic Photodiode and Its Application in Biomedical Devices. *ACS Appl. Electron. Mater.* **2022**, *4* (4), 1567−1575.
(21) Liu, G.; Li, T.; Zhan, X.; Wu, H.; Cao, Y. High-Sensitivity Visible−Near Infrared Organic Photodetectors Based on Non-Fullerene Acceptors. *ACS Appl. Mater. Interfaces* **2020**, *12* (15), 17769−17775.
(22) Xu, C.; Liu, P.; Feng, C.; He, Z.; Cao, Y. Organic photodetectors with high detectivity for broadband detection covering UV-vis-NIR. *J. Mater. Chem. C* **2022**, *10* (15), 5787−5796.
(23) Bong, H.; Lee, W. H.; Lee, D. Y.; Kim, B. J.; Cho, J. H.; Cho, K. High-mobility low-temperature ZnO transistors with low-voltage operation. *Appl. Phys. Lett.* **2010**, *96* (19), No. 192115.
(24) Xie, B.; Xie, R.; Zhang, K.; Yin, Q.; Hu, Z.; Yu, G.; Huang, F.; Cao, Y. Self-filtering narrowband high performance organic photodetectors enabled by manipulating localized Frenkel exciton dissociation. *Nat. Commun.* **2020**, *11* (1), 2871.
(25) Eun, H. J.; Kye, H.; Kim, D.; Jin, I. S.; Jung, J. W.; Ko, S.-J.; Heo, J.; Kim, B.-G.; Kim, J. H. Effective Dark Current Suppression for High-detectivity Organic Near-Infrared Photodetectors Using a Non-Fullerene Acceptor. *ACS Appl. Mater. Interfaces* **2021**, *13* (9), 11144−11150.
(26) Qi, J.; Zhou, X.; Yang, D.; Qiao, W.; Ma, D.; Wang, Z. Y. Optimization of Solubility, Film Morphology and Photodetector Performance by Molecular Side-Chain Engineering of Low-Bandgap Thienothiadiazole-Based Polymers. *Adv. Funct. Mater.* **2014**, *24* (48), 7605−7612.
(27) Su, Z.; Hou, F.; Wang, X.; Gao, Y.; Jin, F.; Zhang, G.; Li, Y.; Zhang, L.; Chu, B.; Li, W. High-Performance Organic Small-Molecule Panchromatic Photodetectors. *ACS Appl. Mater. Interfaces* **2015**, *7* (4), 2529−2534.
(28) Li, P.; Cai, L.; Wang, G.; Zhou, D. C.; Xiang, J.; Zhang, Y. J.; Ding, B. F.; Alameh, K.; Song, Q. L. PEIE capped ZnO as cathode buffer layer with enhanced charge transfer ability for high efficiency polymer solar cells. *Synth. Met.* **2015**, *203*, 243−248.
(29) Wu, J.-L.; Lai, L.-H.; Hsiao, Y.-T.; Tsai, K.-W.; Yang, C.-M.; Sun, Z.-W.; Hsieh, J.-C.; Chang, Y.-M. Top-Illuminated Organic Photodetectors beyond 1000 nm Wavelength Response Enabled by a Well-Defined Interfacial Engineering. *Adv. Opt. Mater.* **2022**, *10* (4), No. 2101723.
(30) Hu, L.; Liu, Y.; Mao, L.; Xiong, S.; Sun, L.; Zhao, N.; Qin, F.; Jiang, Y.; Zhou, Y. Chemical reaction between an ITIC electron acceptor and an amine-containing interfacial layer in non-fullerene solar cells. *J. Mater. Chem. A* **2018**, *6* (5), 2273−2278.
(31) Dong, Y.; Yu, R.; Zhao, B.; Gong, Y.; Jia, H.; Ma, Z.; Gao, H.; Tan, Z. a. Revival of Insulating Polyethylenimine by Creatively Carbonizing with Perylene into Highly Crystallized Carbon Dots as the Cathode Interlayer for High-Performance Organic Solar Cells. *ACS Appl. Mater. Interfaces* **2022**, *14* (1), 1280−1289.
(32) Kim, T.; Kim, J.-H.; Triambulo, R. E.; Han, H.; Park, C.; Park, J.-W. Improving the Stability of Organic−Inorganic Hybrid Perovskite Light-Emitting Diodes Using Doped Electron Transport Materials. *physica status solidi (a)* **2019**, *216* (20), No. 1900426.
(33) Yu, H.; Huang, X.; Huang, C. PEIE doped ZnO as a tunable cathode interlayer for efficient polymer solar cells. *Appl. Surf. Sci.* **2019**, *470*, 318−330.

https://doi.org/10.1021/acsami.4c01466
ACS Appl. Mater. Interfaces 2024, 16, 27576−27586

(34) Zhang, Z.-G.; Qi, B.; Jin, Z.; Chi, D.; Qi, Z.; Li, Y.; Wang, J. Perylene diimides: a thickness-insensitive cathode interlayer for high performance polymer solar cells. *Energy Environ. Sci.* **2014**, *7* (6), 1966−1973.
(35) Moustafa, E.; Méndez, M.; Pallarès, J.; Marsal, L. F. Low temperature based PDINO cathode interlayer for high operational photostable inverted non-fullerene organic solar cells. *Sol. Energy Mater. Sol. Cells* **2022**, *248*, No. 111985.
(36) Kim, M. S.; Jang, W.; Nguyen, T.-Q.; Wang, D. H. Morphology Inversion of a Non-Fullerene Acceptor Via Adhesion Controlled Decal-Coating for Efficient Conversion and Detection in Organic Electronics. *Adv. Funct. Mater.* **2021**, *31* (38), No. 2103705.
(37) Roslan, N. A.; Supangat, A.; Sagadevan, S. Investigation of Charge Transport Properties in VTP: PC71BM Organic Schottky Diode. *Electronics* **2022**, No. 3777.
(38) Le Corre, V. M.; Duijnstee, E. A.; El Tambouli, O.; Ball, J. M.; Snaith, H. J.; Lim, J.; Koster, L. J. A. Revealing Charge Carrier Mobility and Defect Densities in Metal Halide Perovskites via Space-Charge-Limited Current Measurements. *ACS Energy Lett.* **2021**, *6* (3), 1087−1094.
(39) Xu, W.; Khizar ul, H.; Bai, Y.; Jiang, X. Y.; Zhang, Z. L. The estimation of electron mobility of 4,7-diphyenyl-1, 10-phenanthroline using space-charge-limited currents. *Solid State Commun.* **2008**, *146* (7), 311−314.
(40) Li, L.; Zhang, F.; Wang, J.; An, Q.; Sun, Q.; Wang, W.; Zhang, J.; Teng, F. Achieving EQE of 16,700% in P3HT:PC71BM based photodetectors by trap-assisted photomultiplication. *Sci. Rep.* **2015**, *5* (1), 9181.
(41) Lim, E. L.; Yap, C. C.; Hj Jumali, M. H.; Khairulaman, F. L. Solution-dispersed copper iodide anode buffer layer gives P3HT:PCBM-based organic solar cells an efficiency boost. *J. Mater. Sci.: Mater. Electron.* **2019**, *30* (3), 2726−2731.
(42) Sheikh, A. D.; Munir, R.; Haque, M. A.; Bera, A.; Hu, W.; Shaikh, P.; Amassian, A.; Wu, T. Effects of High Temperature and Thermal Cycling on the Performance of Perovskite Solar Cells: Acceleration of Charge Recombination and Deterioration of Charge Extraction. *ACS Appl. Mater. Interfaces* **2017**, *9* (40), 35018−35029.
(43) Perdigón-Toro, L.; Phuong, L. Q.; Eller, F.; Freychet, G.; Saglamkaya, E.; Khan, J. I.; Wei, Q.; Zeiske, S.; Kroh, D.; Wedler, S.; Köhler, A.; Armin, A.; Laquai, F.; Herzig, E. M.; Zou, Y.; Shoaee, S.; Neher, D. Understanding the Role of Order in Y-Series Non-Fullerene Solar Cells to Realize High Open-Circuit Voltages. *Adv. Energy Mater.* **2022**, *12* (12), No. 2103422.
(44) Gasparini, N.; Wadsworth, A.; Moser, M.; Baran, D.; McCulloch, I.; Brabec, C. J. The Physics of Small Molecule Acceptors for Efficient and Stable Bulk Heterojunction Solar Cells. *Adv. Energy Mater.* **2018**, *8* (12), No. 1703298.
(45) Xie, S.; Xia, Y.; Zheng, Z.; Zhang, X.; Yuan, J.; Zhou, H.; Zhang, Y. Effects of Nonradiative Losses at Charge Transfer States and Energetic Disorder on the Open-Circuit Voltage in nonfullerene Organic Solar Cells. *Adv. Funct. Mater.* **2018**, *28* (5), No. 1705659.
(46) Li, C.; Zhou, J.; Song, J.; Xu, J.; Zhang, H.; Zhang, X.; Guo, J.; Zhu, L.; Wei, D.; Han, G.; Min, J.; Zhang, Y.; Xie, Z.; Yi, Y.; Yan, H.; Gao, F.; Liu, F.; Sun, Y. Non-fullerene acceptors with branched side chains and improved molecular packing to exceed 18% efficiency in organic solar cells. *Nat. Energy* **2021**, *6* (6), 605−613.
(47) Wang, S.; Zhang, C.; Feng, Y.; Shao, Y.; Yan, Y.; Dong, Q.; Liu, J.; Hu, B.; Jin, S.; Shi, Y. High-air-flow-velocity assisted intermediate phase engineering for controlled crystallization of mixed perovskite in high efficiency photovoltaics. *J. Mater. Chem. A* **2018**, *6* (19), 8860−8867.
(48) Simone, G.; Dyson, M. J.; Weijtens, C. H. L.; Meskers, S. C. J.; Coehoorn, R.; Janssen, R. A. J.; Gelinck, G. H. On the Origin of Dark Current in Organic Photodiodes. *Adv. Opt. Mater.* **2020**, *8* (1), No. 1901568, DOI: 10.1002/adom.201901568.
(49) Hsiao, P.-H.; Kuo, K.-Y.; Chen, Y.; Wu, T.-Y.; Chen, C.-Y. Balance of photon management and charge collection from carbon-quantum-dot layers as self-powered broadband photodetectors. *Nanoscale Adv.* **2023**, *5* (4), 1086−1094.
(50) Labanti, C.; Wu, J.; Shin, J.; Limbu, S.; Yun, S.; Fang, F.; Park, S. Y.; Heo, C.-J.; Lim, Y.; Choi, T.; Kim, H.-J.; Hong, H.; Choi, B.; Park, K.-B.; Durrant, J. R.; Kim, J.-S. Light-intensity-dependent photoresponse time of organic photodetectors and its molecular origin. *Nat. Commun.* **2022**, *13* (1), 3745.
(51) Xing, Z.; Meng, X.; Sun, R.; Hu, T.; Huang, Z.; Min, J.; Hu, X.; Chen, Y. An Effective Method for Recovering Nonradiative Recombination Loss in Scalable Organic Solar Cells. *Adv. Funct. Mater.* **2020**, *30* (21), No. 2000417.
(52) Huang, J.; Lee, J.; Nakayama, H.; Schrock, M.; Cao, D. X.; Cho, K.; Bazan, G. C.; Nguyen, T.-Q. Understanding and Countering Illumination-Sensitive Dark Current: Toward Organic Photodetectors with Reliable High detectivity. *ACS Nano* **2021**, *15* (1), 1753−1763.
(53) Bhat, G.; Kielar, M.; Sah, P.; Pandey, A. K.; Sonar, P. Solution-Processed Ternary Organic Photodetectors with Ambipolar Small-Bandgap Polymer for Near-Infrared Sensing. *Adv. Electron. Mater.* **2024**, *10* (2), No. 2300583.
(54) Chen, Y.; Zheng, Y.; Jiang, Y.; Fan, H.; Zhu, X. Carbon-Bridged 1,2-Bis(2-thienyl)ethylene: An Extremely Electron Rich Dithiophene Building Block Enabling Electron Acceptors with Absorption above 1000 nm for Highly Sensitive NIR Photodetectors. *J. Am. Chem. Soc.* **2021**, *143* (11), 4281−4289.
(55) Lee, U.-H.; Park, B.; Rhee, S.; Ha, J.-W.; Whang, D. R.; Eun, H. J.; Kim, J. H.; Shim, Y.; Heo, J.; Lee, C.; Kim, B. J.; Yoon, S. C.; Lee, J.; Ko, S.-J. Achieving Highly Sensitive Near-Infrared Organic Photodetectors using Asymmetric Non-Fullerene Acceptor. *Adv. Opt. Mater.* **2023**, *11* (17), No. 2300312.
(56) Ha, J.-W.; Lee, A. Y.; Eun, H. J.; Kim, J.-H.; Ahn, H.; Park, S.; Lee, C.; Seo, D. W.; Heo, J.; Yoon, S. C.; Ko, S.-J.; Kim, J. H. High detectivity Near Infrared Organic Photodetectors Using an Asymmetric Non-Fullerene Acceptor for Optimal Nanomorphology and Suppressed Dark Current. *ACS Nano* **2023**, *17* (19), 18792−18804.
(57) Liu, T.; Jia, Z.; Song, Y.; Yu, N.; Lin, Q.; Li, C.; Jia, Y.; Chen, H.; Wang, S.; Wei, Y.; Lin, Y.; Huang, F.; Tang, Z.; Li, Y.; Meng, L.; Huang, H. Near Infrared Self-Powered Organic Photodetectors with a Record Responsivity Enabled by Low Trap Density. *Adv. Funct. Mater.* **2023**, *33* (25), No. 2301167.
(58) Wang, J.; Deng, S.; Hu, J.; Miao, J.; Li, J.; Liu, J.; Liu, Y. Alcohol-Soluble n-Type Polythiophenes as Cathode Interlayer in Organic Photodetectors for Hole Blocking. *Adv. Funct. Mater.* **2024**, No. 2312502.
(59) Lee, P.-H.; Wu, T.-T.; Li, C.-F.; Glowienka, D.; Huang, Y.-X.; Huang, S.-H.; Huang, Y.-C.; Su, W.-F. Featuring Semitransparent p−i−n Perovskite Solar Cells for High-Efficiency Four-Terminal/Silicon Tandem Solar Cells. *Sol. RRL* **2022**, *6* (4), No. 2100891.
(60) Yan, T.; Li, Z.; Cao, F.; Chen, J.; Wu, L.; Fang, X. An All-Organic Self-Powered Photodetector with Ultraflexible Dual-Polarity Output for Biosignal Detection. *Adv. Mater.* **2022**, *34* (30), No. 2201303.
(61) Jang, W.; Kim, B. G.; Seo, S.; Shawky, A.; Kim, M. S.; Kim, K.; Mikladal, B.; Kauppinen, E. I.; Maruyama, S.; Jeon, I.; Wang, D. H. Strong dark current suppression in flexible organic photodetectors by carbon nanotube transparent electrodes. *Nano Today* **2021**, *37*, No. 101081.